Available online at www.sciencedirect.com
ScienceDirect
Journal of Sound and Vibration 318 (2008) 592–605
JOURNAL OF SOUND AND VIBRATION
www.elsevier.com/locate/jsvi

An impulsive receptance technique for the time domain computation of the vibration of a whole aero-engine model with nonlinear bearings

Pham Minh Hai, Philip Bonello*

School of Mechanical, Aerospace and Civil Engineering, University of Manchester, Manchester M60 1QD, UK

Received 6 March 2008; received in revised form 15 April 2008; accepted 16 April 2008
Handling Editor: M.P. Cartmell
Available online 20 June 2008

Abstract

The direct study of the vibration of real engine structures with nonlinear bearings, particularly aero-engines, has been severely limited by the fact that current nonlinear computational techniques are not well-suited for complex large-order systems. This paper introduces a novel implicit "impulsive receptance method" (IRM) for the time domain analysis of such structures. The IRM's computational efficiency is largely immune to the number of modes used and dependent only on the number of nonlinear elements. This means that, apart from retaining numerical accuracy, a much more physically accurate solution is achievable within a short timeframe. Simulation tests on a realistically sized representative twin-spool aero-engine showed that the new method was around 40 times faster than a conventional implicit integration scheme. Preliminary results for a given rotor unbalance distribution revealed the varying degree of journal lift, orbit size and shape at the example engine's squeeze-film damper bearings, and the effect of end-sealing at these bearings.

1. Introduction

Most aero-engine assemblies are complex structures involving at least two nested rotors mounted within a flexible casing via squeeze-film damper (SFD) bearings. Most SFDs are unsupported, as can be seen in Fig. 1, where a parallel retainer spring is only used with one SFD at the end of each rotor, to provide axial location. The deployment of SFDs into such structures is highly cost effective but requires careful calculation since they can be highly nonlinear in their performance, particularly when unsupported [1]. Various techniques have been proposed by academia for the computation of the unbalance vibration of simple rotor/nonlinear bearing systems. However, such tools are not well-suited for complex systems that have many degrees of freedom, thereby severely limiting the direct study of real engine structures. This is evidenced by the fact that there exists little, if any, published research on the computational analysis of such structures. Indeed, proposed

*Corresponding author.
E-mail address: philip.bonello@manchester.ac.uk (P. Bonello).

0022-460X/$ - see front matter © 2008 Elsevier Ltd. All rights reserved.
doi:10.1016/j.jsv.2008.04.033

Nomenclature

$\mathbf{a}$, $\mathbf{b}$ $= [a_1 \ \dots \ a_n]^{\mathrm{T}}$, $[b_1 \ \dots \ b_n]^{\mathrm{T}}$

$\mathbf{a.*b}$ $= [a_1 b_1 \ \dots \ a_n b_n]^{\mathrm{T}}$

$\mathbf{a./b}$ $= [a_1/b_1 \ \dots \ a_n/b_n]^{\mathrm{T}}$

$\mathbf{a.}^p$ $= [a_1^p \ \cdots \ a_n^p]^{\mathrm{T}}$

$\sin(\mathbf{a})$ $= [\sin a_1 \ \cdots \ \sin a_n]^{\mathrm{T}}$

$\cos(\mathbf{a})$ $= [\cos a_1 \ \cdots \ \cos a_n]^{\mathrm{T}}$

$\mathbf{f}$ vector of squeeze-film forces, unbalance forces, static loading (Eq. (3))

$\mathbf{f}_k$ $= \mathbf{f}(\mathbf{x}_k, \dot{\mathbf{x}}_k, t_k)$

$\mathbf{g}$ $= \{\mathbf{g}^{(j)}\} = [\mathbf{g}^{(1)\mathrm{T}} \cdots \mathbf{g}^{(J)\mathrm{T}}]^{\mathrm{T}}$

$\mathbf{g}^{(j)}$ $= [\, M_1^{(j)} \quad N_1^{(j)} \quad \cdots \quad M_{G_j}^{(j)} \quad N_{G_j}^{(j)} \,]^{\mathrm{T}}$

$\mathbf{g}_k$ $= \mathbf{g}(t_k)$

G_j total number of gyroscopic locations on rotor no. j

h time step size

$\mathbf{H_f}$, $\mathbf{H_x}$, $\mathbf{H_\theta}$, $\mathbf{H_g}$ modal matrices defined in Eqs. (2, 5, 18, 19, 27a, 27b)

i counter for nonlinear bearings

$I_p^{(j)}$ polar moment of inertia at gyroscopic location no. p of rotor no. j

$\mathbf{I}$ identity matrix

j counter for rotors

J total number of rotors

k time-step counter ($= 0,1,\dots$)

$\mathbf{L}$ matrix defined by Eq. (29a)

$M_p^{(j)}$, $N_p^{(j)}$ gyroscopic moments about x, y axes, respectively, at gyroscopic location no. p of rotor no. j

$\mathbf{n}$ vector of ones

p counter for concentrated gyroscopic effect location

P total number of rigid-body modes

$\mathbf{P}$ block diagonal matrix of diagonal submatrices $\mathbf{P}^{(j)}$, $j = 1,\dots,J$

$$\mathbf{P}^{(j)} = \Omega^{(j)}\,\mathbf{diag}\{-I_1^{(j)}, I_1^{(j)}, \dots, -I_{G_j}^{(j)}, I_{G_j}^{(j)}\} = \Omega^{(j)} \begin{bmatrix} -I_1^{(j)} & 0 \cdots & \vdots \\ 0 & \ddots & 0 \\ \vdots & \cdots 0 & I_{G_j}^{(j)} \end{bmatrix}$$

$\mathbf{q}$ vector of modal coordinates (Eq. (1))

$\mathbf{q}_k$, $\dot{\mathbf{q}}_k$ $= \mathbf{q}(t_k)$, $\dot{\mathbf{q}}_k(t_k)$

$\hat{\mathbf{q}}_k$, $\hat{\dot{\mathbf{q}}}_k$ defined by Eqs. (9 or 21)

r counter for modes

R total number of modes considered

$\mathbf{R_{xf}}, \mathbf{S_{xf}}$ matrices defined by Eqs. (13, 22)

$\mathbf{R_{xg}}$, $\mathbf{S_{xg}}$, $\mathbf{S_{\theta f}}$, $\mathbf{S_{\theta g}}$ matrices obtained analogously to $\mathbf{R_{xf}}$, $\mathbf{S_{xf}}$

$\mathbf{s}$ vector of state variables $\mathbf{q}$, $\dot{\mathbf{q}}$ (Section 3.2.1)

t time

t_k discrete time, $= t_{k-1} + h$ for $k = 1,2, \dots$

$\mathbf{T}$ matrix defined by Eq. (29b)

$\mathbf{v}_i$ vector of relative Cartesian displacements at terminals of squeeze-film no. i (Eq. (31))

$\mathbf{v}_{\mathrm{s},i}$ vector of static Cartesian offsets at squeeze-film no. i

$\mathbf{x}$ vector of dynamic Cartesian displacements at the squeeze-films, Eq. (32)

$\mathbf{x}_k$, $\dot{\mathbf{x}}_k$ $= \mathbf{x}(t_k)$, $\dot{\mathbf{x}}(t_k)$

$\hat{\mathbf{x}}_k$, $\hat{\dot{\mathbf{x}}}_k$, defined by Eqs. (11)

$x_{\mathrm{d},i}$, $y_{\mathrm{d},i}$ dynamic part of $\mathbf{v}_i$, Eq. (31)

x, y, z Cartesian frame, Fig. 1

$[\,]^{\mathrm{T}}$ matrix/vector transpose

$[\tilde{\ }]$ modal parameters pertaining to flexible modes

$[\bar{\ }]$ modal parameters pertaining to rigid-body modes

$[\dot{\ }]$ d()/dt

Greek letters

$\alpha_p^{(j)}$, $\beta_p^{(j)}$ rotational deformation about x, y axes, respectively, at gyroscopic location no. p of rotor no. j

$\boldsymbol{\theta}$ $= \{\boldsymbol{\theta}^{(j)}\} = [\boldsymbol{\theta}^{(1)\mathrm{T}} \ \cdots \ \boldsymbol{\theta}^{(J)\mathrm{T}}]$

$\boldsymbol{\theta}^{(j)}$ $= [\, \beta_1^{(j)} \quad \alpha_1^{(j)} \quad \cdots \quad \beta_{G_j}^{(j)} \quad \alpha_{G_j}^{(j)} \,]^{\mathrm{T}}$

$\dot{\boldsymbol{\theta}}_k$ $= \dot{\boldsymbol{\theta}}(t_k)$

$\hat{\dot{\boldsymbol{\theta}}}_k$ defined by Eq. (26b)

λ end-leakage factor of a squeeze-film damper (Ref. [12])

τ local time over interval $[t_{k-1}, t_k]$

$\boldsymbol{\omega}$ vector of natural circular frequencies in Eq. (1)

$\boldsymbol{\psi}_{\mathbf{x}}^{(r)}$ value of $\mathbf{x}$ in rth mass-normalised mode

$\boldsymbol{\psi}_{\mathbf{f}}^{(r)}$, $\boldsymbol{\psi}_{\mathbf{g}}^{(r)}$ mass-normalised eigenvectors evaluated at degrees of freedom corresponding to directions and locations of elements in $\mathbf{f}$, $\mathbf{g}$

$\boldsymbol{\psi}_{\boldsymbol{\theta}}^{(r)}$ mass-normalised eigenvectors evaluated at degrees of freedom in $\boldsymbol{\theta}$

$\Omega^{(j)}$ rotational speed of rotor no. j (rad/s)

$\boldsymbol{\rho}$ $= \{\boldsymbol{\rho}_i\} = [\boldsymbol{\rho}_1^{\mathrm{T}} \cdots \boldsymbol{\rho}_5^{\mathrm{T}}]^{\mathrm{T}}$

$\boldsymbol{\rho}_i$ $= [\, Q_{x_i} \quad Q_{y_i} \,]^{\mathrm{T}}$ (Cartesian forces on journal at squeeze-film no. i)

$\boldsymbol{\chi}$ vector function of $\mathbf{s}$ and t (Section 3.2.1)

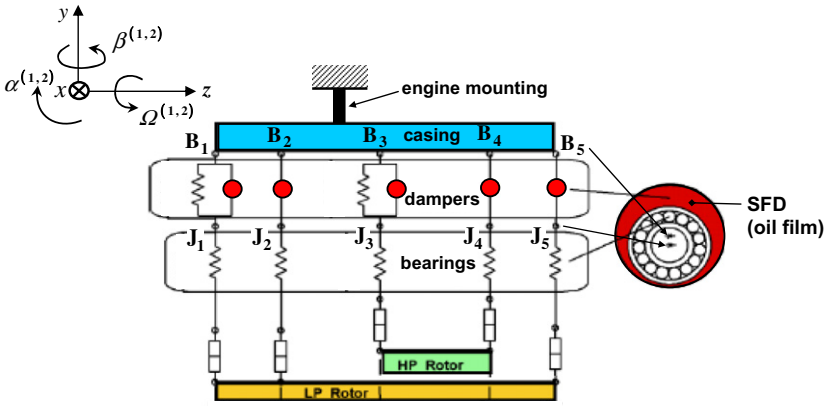

Fig. 1. Schematic of a representative twin-spool engine. (LP: "low pressure", HP: "high pressure").

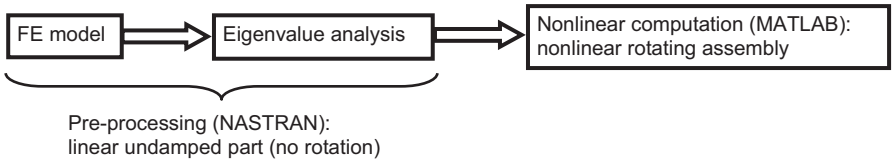

Fig. 2. Overall computational procedure.

computational techniques, although ostensibly generic, have almost invariably been illustrated on simple rotor-bearing systems e.g. Refs. [2–7].

This paper presents the first stage of a project aimed at the development and validation of a suite of computational techniques for unbalance response computation, suitable for generic whole-engine models, which will significantly extend the capability of current finite element (FE) packages. The proposed analysis of the nonlinear rotating assembly uses the modal parameters of the undamped linear part of the assembly under non-rotating conditions. Implementation is possible through the integration of Nastran®, used for the linear pre-processing, and specially written Matlab® routines for the subsequent nonlinear computation (Fig. 2).

Owing to the complementary nature and relative merits of time and frequency domain solution techniques [6] both approaches were developed for the nonlinear computation part. Frequency domain techniques, most notably harmonic balance (HB), are inherently much faster since they directly yield steady-state solutions that are assumed to be periodic at an assumed fundamental frequency. However, such periodic vibration is not always physically possible since a nonlinear system subjected to periodic external excitation (e.g. rotor unbalance) is capable of non-periodic steady-state vibration. In such a case, a time-marching technique is used, which yields the actual steady-state response after the initial transients have died out. Moreover, in order to start off a HB solution procedure over a range of speeds, a good initial approximation at just one speed is required. This can only be reliably provided by a time domain solution, especially for a large order system [6].

This paper will focus on the development of the time domain solution for the nonlinear response. It is to be mentioned that, although major FE packages have a time domain solver facility, this is considered by the authors to be very restrictive in two ways: (i) limitations on the choice of the model for the nonlinear bearing element (if one is available); (ii) unsuitability of the solution technique for the problem at hand due to the issues described in the following part of this section.

When dealing with large-order systems, the direct integration of the FE equations is highly time-consuming and so, is generally avoided [8]. For such applications, two alternative time-saving model-reduction approaches have been proposed in the literature. One approach is to model the system using transfer matrices e.g. Ref. [3]. This technique is an alternative to the FE approach of modelling the structure. Unlike FE,

transfer matrices are not suited for modelling complex sub-systems such as the engine casing. For this reason, the transfer matrix approach has not crossed over to whole-engine modelling. The other approach, which is preferred since it exploits the modelling capability of FE, is to transform the FE problem into modal space and retain only a limited number of modal equations of motion [8]. In either approach, the resulting equations are solved by a time-marching scheme. Due to problems of "numerical stiffness" [9], implicit time-marching techniques are preferred. An implicit "fast integration scheme" based on the trapezoidal rule of integration, was presented in Ref. [4] and shown to be much faster than the (explicit) Runge–Kutta technique when applied to a simple flexible rotor system with one SFD. At around the same time, Matlab introduced a whole suite of solvers suitable for stiff systems, based on more sophisticated rules such as the modified Rosenbrock method used in solver *ode23s*©[9]. This solver was used extensively in Refs. [6,7] where the modal equations of motion of various test rigs were integrated. In Ref. [5], the modal equations of motion of a rotor-bearing system were integrated using an iterative predictor–corrector scheme combining the Central Difference and Newmark–Beta methods. The system considered there was a gas turbine rotor mounted on two bearing pedestals simplified as mass–spring systems.

Conventional implicit integration schemes transform the differential equations of motion into an equal number of algebraic equations which then have to be solved at each time step to obtain the current state variables. Moreover, if the system contains nonlinear motion-dependent forces, then this solution has to be obtained by iteration. As shall be shown in this paper, with a real engine a modal transformation would still necessitate the retention of a very large number of modes. Hence, due to the large number of modal equations, the time-marching process slows down to impractical levels. For this reason, in order to analyse an aero-engine, a novel implicit "impulsive receptance method" (IRM) was developed.

The choice of the name for the method derives from the fact that the structural response at a certain degree of freedom due to unit impulse in another degree of freedom is termed in Ref. [10] as the "impulsive receptance" connecting the two degrees of freedom. This quantity is also the inverse Fourier transform of the corresponding frequency response function (receptance). The IRM equations derived in this paper are essentially the inverse Fourier transform of the frequency domain receptance/mobility equations relating the relative displacements and velocities at the SFDs with the motion-dependent forces and other excitations acting on the linear part of the structure. Hence, the IRM's computational efficiency is largely immune to the number of modes used and dependent only on the number of nonlinear elements. This means that, apart from retaining numerical accuracy, a much more physically accurate solution is achievable within a short timeframe.

In the following section, the theory of the IRM is presented. In Section 3, the method is tested on a realistically sized representative twin-spool aero-engine model and validated against a conventional technique. The results of a preliminary parametric analysis are also presented.

2. Theory

2.1. Outline

The following notation for operations on vectors (i.e. column matrices) shall be adopted: if $\mathbf{a} = [a_1 \ \dots \ a_n]^{\mathrm{T}}$, $\mathbf{b} = [b_1 \ \dots \ b_n]^{\mathrm{T}}$, then $\mathbf{a}.*\mathbf{b} = [a_1 b_1 \ \dots \ a_n b_n]^{\mathrm{T}}$, $\mathbf{a}./\mathbf{b} = \mathbf{a}.*\mathbf{b} = [a_1/b_1 \ \dots \ a_n/b_n]^{\mathrm{T}}$, $\mathbf{a}.^p = [a_1^p \ \cdots \ a_n^p]^{\mathrm{T}}$, $\sin(\mathbf{a}) = [\sin a_1 \ \cdots \ \sin a_n]^{\mathrm{T}}$, etc. This notation is borrowed from Matlab [11] and allows not only the compact expression of the theory, but highly efficient computational implementation.

The modal parameters in all the theory pertain to the linear part of the assembly under non-rotating conditions. By "linear part" is meant the structure that remains in Fig. 1 when the SFDs are replaced by gaps. The damping in the linear part of an engine is commonly regarded as negligible, but the following analysis can be modified to accommodate proportional damping in the linear part at no computational cost. The gyroscopic effect is neglected in this sub-section but is considered in Section 2.3.

The equations of motion in modal space are

$$\ddot{\mathbf{q}} + (\boldsymbol{\omega}.^2).*\mathbf{q} = \mathbf{H}_{\mathbf{f}}^{\mathrm{T}}\mathbf{f} \tag{1}$$

In Eq. (1), $\mathbf{q}$ is the $R \times 1$ vector of modal coordinates, $\boldsymbol{\omega}$ the vector of natural frequencies, and $\mathbf{H}_{\mathbf{f}}$ the matrix of mass-normalised eigenvectors $\boldsymbol{\psi}_{\mathbf{f}}^{(r)}$ $(r = 1,\dots,R)$ taken at the degrees of freedom corresponding to the

directions and locations of the elements of **f**:

$$\mathbf{H_f} = \left[\boldsymbol{\psi}_\mathbf{f}^{(1)} \quad \cdots \quad \boldsymbol{\psi}_\mathbf{f}^{(R)} \right] \tag{2}$$

f contains the forces external to the linear part: squeeze-film forces, unbalance forces, static forces. The inertia of the fluid films at the bearings is commonly regarded as negligible (e.g. Refs. [2–7]). Hence, one can write

$$\mathbf{f} = \mathbf{f}(\mathbf{x}, \dot{\mathbf{x}}, t) \tag{3}$$

where $\mathbf{x}, \dot{\mathbf{x}}$ are the vectors of the relative x, y dynamic displacements and velocities, respectively, at the squeeze-film terminals (i.e. journal centre J_i relative to housing centre B_i, $i = 1,\ldots,5$ in Fig. 1):

$$\mathbf{x} = \mathbf{H_x}\mathbf{q}, \quad \dot{\mathbf{x}} = \mathbf{H_x}\dot{\mathbf{q}} \tag{4a,b}$$

$\mathbf{H_x}$ being the matrix whose columns $\boldsymbol{\psi}_\mathbf{x}{}^{(r)}$ define the values of **x** in the respective mass-normalised modes:

$$\mathbf{H_x} = \left[\boldsymbol{\psi}_\mathbf{x}^{(1)} \quad \cdots \quad \boldsymbol{\psi}_\mathbf{x}^{(R)} \right] \tag{5}$$

The $\boldsymbol{\psi}_\mathbf{x}{}^{(r)}$ are loosely referred to here as "eigenvectors". They are in fact the difference of the eigenvectors $\boldsymbol{\psi}_\mathbf{J}{}^{(r)}$, $\boldsymbol{\psi}_\mathbf{B}{}^{(r)}$ defining the x, y displacements of J_i, B_i in mode no. r.

Let $\mathbf{q}_k = \mathbf{q}(t_k)$ and $\dot{\mathbf{q}}_k = \dot{\mathbf{q}}(t_k)$. $\mathbf{q}_k$, $\dot{\mathbf{q}}_k$ are unknown whereas $\mathbf{q}_{k-1}$, $\dot{\mathbf{q}}_{k-1}$ are known. Using the Duhamel integral method [8] over the interval $[t_{k-1}, t_k]$, where $t_k = t_{k-1} + h$:

$$\mathbf{q}_k = \dot{\mathbf{q}}_{k-1}.*\sin(\boldsymbol{\omega}h)./\boldsymbol{\omega} + \mathbf{q}_{k-1}.*\cos(\boldsymbol{\omega}h) + \int_0^h \left\{\mathbf{H}_\mathbf{f}^\mathrm{T}\mathbf{f}(\tau)\right\}.*\sin(\boldsymbol{\omega}h - \boldsymbol{\omega}\tau)./\boldsymbol{\omega}\,\mathrm{d}\tau \tag{6a}$$

$$\dot{\mathbf{q}}_k = \dot{\mathbf{q}}_{k-1}.*\cos(\boldsymbol{\omega}h) - \mathbf{q}_{k-1}.*\boldsymbol{\omega}.*\sin(\boldsymbol{\omega}h) + \int_0^h \left\{\mathbf{H}_\mathbf{f}^\mathrm{T}\mathbf{f}(\tau)\right\}.*\cos(\boldsymbol{\omega}h - \boldsymbol{\omega}\tau)\,\mathrm{d}\tau \tag{6b}$$

Over the interval $0 \leqslant \tau \leqslant h$, $\mathbf{f}(\tau)$ is approximated as

$$\mathbf{f}(\tau) = \mathbf{f}_{k-1} + (\mathbf{f}_k - \mathbf{f}_{k-1})\frac{\tau}{h} \tag{7}$$

where $\mathbf{f}_k = \mathbf{f}(\mathbf{x}_k, \dot{\mathbf{x}}_k, t_k)$ and $\mathbf{x}_k = \mathbf{x}(t_k), \dot{\mathbf{x}}_k = \dot{\mathbf{x}}(t_k)$. Hence, after substituting Eq. (7) into Eqs. (6a,b), expanding the trigonometric functions under the integral signs, evaluating the resulting integrals and simplifying, one obtains:

$$\mathbf{q}_k = \hat{\mathbf{q}}_k + (\mathbf{H}_\mathbf{f}^\mathrm{T}\mathbf{f}_k - \mathbf{H}_\mathbf{f}^\mathrm{T}\mathbf{f}_{k-1}).*\left\{\boldsymbol{\omega} - \frac{1}{h}\sin(\boldsymbol{\omega}h)\right\}./(\boldsymbol{\omega}.^3) \tag{8a}$$

$$\dot{\mathbf{q}}_k = \hat{\dot{\mathbf{q}}}_k + (\mathbf{H}_\mathbf{f}^\mathrm{T}\mathbf{f}_k - \mathbf{H}_\mathbf{f}^\mathrm{T}\mathbf{f}_{k-1}).*\{\mathbf{n} - \cos(\boldsymbol{\omega}h)\}./(h\boldsymbol{\omega}.^2) \tag{8b}$$

where

$$\hat{\mathbf{q}}_k = \dot{\mathbf{q}}_{k-1}.*\sin(\boldsymbol{\omega}h)./\boldsymbol{\omega} + \mathbf{q}_{k-1}.*\cos(\boldsymbol{\omega}h) + \mathbf{H}_\mathbf{f}^\mathrm{T}\mathbf{f}_{k-1}.*\{\mathbf{n} - \cos(\boldsymbol{\omega}h)\}./(\boldsymbol{\omega}.^2) \tag{9a}$$

$$\hat{\dot{\mathbf{q}}}_k = \dot{\mathbf{q}}_{k-1}.*\cos(\boldsymbol{\omega}h) - \mathbf{q}_{k-1}.*\boldsymbol{\omega}.*\sin(\boldsymbol{\omega}h) + \mathbf{H}_\mathbf{f}^\mathrm{T}\mathbf{f}_{k-1}.*\sin(\boldsymbol{\omega}h)./\boldsymbol{\omega} \tag{9b}$$

In Eqs. (8b, 9a), **n** is a vector of ones ("1's") of the appropriate size. Multiplying both sides of Eqs. (8a) and (8b) by $\mathbf{H_x}$ and noting Eqs. (4a,b):

$$\mathbf{x}_k = \hat{\mathbf{x}}_k + \mathbf{H_x}\left[\left\{\mathbf{H}_\mathbf{f}^\mathrm{T}(\mathbf{f}_k - \mathbf{f}_{k-1})\right\}.*\left\{\boldsymbol{\omega} - \frac{1}{h}\sin(\boldsymbol{\omega}h)\right\}./(\boldsymbol{\omega}.^3)\right] \tag{10a}$$

$$\dot{\mathbf{x}}_k = \hat{\dot{\mathbf{x}}}_k + \mathbf{H_x}\left[\left\{\mathbf{H}_\mathbf{f}^\mathrm{T}(\mathbf{f}_k - \mathbf{f}_{k-1})\right\}.*\{\mathbf{n} - \cos(\boldsymbol{\omega}h)\}./(h\boldsymbol{\omega}.^2)\right] \tag{10b}$$

where

$$\hat{\mathbf{x}}_k = \mathbf{H_x}\hat{\mathbf{q}}_k, \ \hat{\dot{\mathbf{x}}}_k = \mathbf{H_x}\hat{\dot{\mathbf{q}}}_k \tag{11a,b}$$

Eqs. (10a,b) can be simplified to

$$\mathbf{x}_k = \hat{\mathbf{x}}_k + \mathbf{R}_{\mathbf{xf}}(h)\{\mathbf{f}_k(\mathbf{x}_k, \dot{\mathbf{x}}_k, t_k) - \mathbf{f}_{k-1}\} \tag{12a}$$

$$\dot{\mathbf{x}}_k = \hat{\dot{\mathbf{x}}}_k + \mathbf{S}_{\mathbf{xf}}(h)\{\mathbf{f}_k(\mathbf{x}_k, \dot{\mathbf{x}}_k, t_k) - \mathbf{f}_{k-1}\} \tag{12b}$$

where the discrete time domain analogues of the receptance and mobility matrices are given by

$$\mathbf{R}_{\mathbf{xf}}(h) = \sum_{r=1}^{R}\left\{\boldsymbol{\psi}_{\mathbf{x}}^{(r)}\boldsymbol{\psi}_{\mathbf{f}}^{(r)\mathrm{T}}\left(\boldsymbol{\omega}_r - \frac{1}{h}\sin\,\omega_r h\right)\Big/\omega_r^3\right\},\ \mathbf{S}_{\mathbf{xf}}(h) = \sum_{r=1}^{R}\left\{\boldsymbol{\psi}_{\mathbf{x}}^{(r)}\boldsymbol{\psi}_{\mathbf{f}}^{(r)\mathrm{T}}(1-\cos\,\omega_r h)/(h\omega_r^2)\right\} \tag{13a,b}$$

Eqs. (12a, b) are a set of nonlinear algebraic equations with $\mathbf{x}_k, \dot{\mathbf{x}}_k$ as unknowns. Hence, one can use an iterative method to solve for $\mathbf{x}_k, \dot{\mathbf{x}}_k$. *The number of* equations to *be solved is hence only four times the number of SFDs*. From Eqs. (12a, b), the initial approximation can be taken as $\mathbf{x}_k \approx \hat{\mathbf{x}}_k,\ \dot{\mathbf{x}}_k \approx \hat{\dot{\mathbf{x}}}_k$. Once $\mathbf{x}_k, \dot{\mathbf{x}}_k$ are found, $\mathbf{f}_k$ is determined, hence from Eqs. (8a, b) one can determine $\mathbf{q}_k, \dot{\mathbf{q}}_k$ and progress the solution.

2.2. Modification for rigid-body modes

Some of the above expressions need to be modified to account for the presence of rigid-body modes since, in the *linear part* of Fig. 1, each rotor is supported at only one point (J_1 or J_3) about which it is free to pivot. The rigid-body mode expressions are obtained by taking the limit $\boldsymbol{\omega}\to\mathbf{0}$. From Eqs. (9a, b), one can show that

$$\lim_{\boldsymbol{\omega}\to\mathbf{0}}\hat{\mathbf{q}}_k = h\dot{\mathbf{q}}_{k-1} + \mathbf{q}_{k-1} + \frac{h^2}{2}\mathbf{H}_{\mathbf{f}}^{\mathrm{T}}\mathbf{f}_{k-1},\ \lim_{\boldsymbol{\omega}\to\mathbf{0}}\hat{\dot{\mathbf{q}}}_k = \dot{\mathbf{q}}_{k-1} + h\mathbf{H}_{\mathbf{f}}^{\mathrm{T}}\mathbf{f}_{k-1} \tag{14a,b}$$

Also, from Eqs. (13a, b),

$$\lim_{\boldsymbol{\omega}\to\mathbf{0}}\mathbf{R}_{\mathbf{xf}}(h) = \frac{h^2}{6}\mathbf{H}_{\mathbf{x}}\mathbf{H}_{\mathbf{f}}^{\mathrm{T}} \quad \text{and} \quad \lim_{\boldsymbol{\omega}\to\mathbf{0}}\mathbf{S}_{\mathbf{xf}}(h) = \frac{h}{2}\mathbf{H}_{\mathbf{x}}\mathbf{H}_{\mathbf{f}}^{\mathrm{T}} \tag{15a,b}$$

From Eqs. (8a, b):

$$\lim_{\boldsymbol{\omega}\to\mathbf{0}}\mathbf{q}_k = \lim_{\boldsymbol{\omega}\to\mathbf{0}}\hat{\mathbf{q}}_k + \frac{h^2}{6}(\mathbf{H}_{\mathbf{f}}^{\mathrm{T}}\mathbf{f}_k - \mathbf{H}_{\mathbf{f}}^{\mathrm{T}}\mathbf{f}_{k-1}),\ \lim_{\boldsymbol{\omega}\to\mathbf{0}}\dot{\mathbf{q}}_k = \lim_{\boldsymbol{\omega}\to\mathbf{0}}\hat{\dot{\mathbf{q}}}_k + \frac{h}{2}(\mathbf{H}_{\mathbf{f}}^{\mathrm{T}}\mathbf{f}_k - \mathbf{H}_{\mathbf{f}}^{\mathrm{T}}\mathbf{f}_{k-1}) \tag{16a,b}$$

If the system has P rigid-body modes, the modal parameters and coordinates are given by

$$\boldsymbol{\omega} = \begin{bmatrix}\mathbf{0}\\ \tilde{\boldsymbol{\omega}}\end{bmatrix},\ \mathbf{H}_{\mathbf{f}} = \begin{bmatrix}\check{\mathbf{H}}_{\mathbf{f}} & \tilde{\mathbf{H}}_{\mathbf{f}}\end{bmatrix},\ \mathbf{H}_{\mathbf{x}} = \begin{bmatrix}\check{\mathbf{H}}_{\mathbf{x}} & \tilde{\mathbf{H}}_{\mathbf{x}}\end{bmatrix},\ \mathbf{q} = \begin{bmatrix}\check{\mathbf{q}}\\ \tilde{\mathbf{q}}\end{bmatrix} \tag{17–20}$$

where $\boldsymbol{\omega}$ has a P-length sub-vector of zeros, $\check{\mathbf{H}}_{\mathbf{f,x}}$ contain the eigenvectors of the rigid-body modes, $\tilde{\mathbf{H}}_{\mathbf{f,x}}$, $\tilde{\boldsymbol{\omega}}$ contain the flexible mode parameters, and $\check{\mathbf{q}}$, $\tilde{\mathbf{q}}$ respectively denote the sub-vectors of rigid and flexible modal coordinates. Eqs. (12a, b), (13a, b), (8a, b) and (9a, b) are then modified as follows, by combining the above rigid-body expressions with the flexible mode expressions of the previous section:

$$\hat{\mathbf{q}}_k = \begin{bmatrix} h\check{\dot{\mathbf{q}}}_{k-1} + \check{\mathbf{q}}_{k-1} + \frac{h^2}{2}\check{\mathbf{H}}_{\mathbf{f}}^{\mathrm{T}}\mathbf{f}_{k-1} \\ \tilde{\dot{\mathbf{q}}}_{k-1}.*\sin(\tilde{\boldsymbol{\omega}}h)./\tilde{\boldsymbol{\omega}} + \tilde{\mathbf{q}}_{k-1}.*\cos(\tilde{\boldsymbol{\omega}}h) + \tilde{\mathbf{H}}_{\mathbf{f}}^{\mathrm{T}}\mathbf{f}_{k-1}.*\{\mathbf{n} - \cos(\tilde{\boldsymbol{\omega}}h)\}./(\tilde{\boldsymbol{\omega}}.^{\mathbf{2}}) \end{bmatrix} \tag{21a}$$

$$\hat{\dot{\mathbf{q}}}_k = \begin{bmatrix} \check{\dot{\mathbf{q}}}_{k-1} + h\check{\mathbf{H}}_{\mathbf{f}}^{\mathrm{T}}\mathbf{f}_{k-1} \\ \tilde{\dot{\mathbf{q}}}_{k-1}.*\cos(\tilde{\boldsymbol{\omega}}h) - \tilde{\mathbf{q}}_{k-1}.*\tilde{\boldsymbol{\omega}}.*\sin(\tilde{\boldsymbol{\omega}}h) + \tilde{\mathbf{H}}_{\mathbf{f}}^{\mathrm{T}}\mathbf{f}_{k-1}.*\sin(\tilde{\boldsymbol{\omega}}h)./\tilde{\boldsymbol{\omega}} \end{bmatrix} \tag{21b}$$

$$\mathbf{R}_{\mathbf{xf}}(h) = \frac{h^2}{6}\check{\mathbf{H}}_{\mathbf{x}}\check{\mathbf{H}}_{\mathbf{f}}^{\mathrm{T}} + \sum_{r=P+1}^{R}\left\{\boldsymbol{\psi}_{\mathbf{x}}^{(r)}\boldsymbol{\psi}_{\mathbf{f}}^{(r)\mathrm{T}}\left(\omega_r - \frac{1}{h}\sin\,\omega_r h\right)\Big/\omega_r^3\right\} \tag{22a}$$

$$\mathbf{S}_{\mathbf{xf}}(h) = \frac{h}{2}\breve{\mathbf{H}}_{\mathbf{x}}\breve{\mathbf{H}}_{\mathbf{f}}^{\mathrm{T}} + \sum_{r=P+1}^{R} \{\boldsymbol{\psi}_{\mathbf{x}}^{(r)}\boldsymbol{\psi}_{\mathbf{f}}^{(r)\mathrm{T}}(1-\cos\,\omega_r h)(h\omega_r^2)\} \tag{22b}$$

$$\mathbf{q}_k = \hat{\mathbf{q}}_k + \begin{bmatrix} \frac{h^2}{6}\left(\breve{\mathbf{H}}_{\mathbf{f}}^{\mathrm{T}}\mathbf{f}_k - \breve{\mathbf{H}}_{\mathbf{f}}^{\mathrm{T}}\mathbf{f}_{k-1}\right) \\ (\tilde{\mathbf{H}}_{\mathbf{f}}^{\mathrm{T}}\mathbf{f}_k - \tilde{\mathbf{H}}_{\mathbf{f}}^{\mathrm{T}}\mathbf{f}_{k-1}).*\left\{\tilde{\omega} - \frac{1}{h}\sin(\tilde{\boldsymbol{\omega}}h)\right\}./(\tilde{\boldsymbol{\omega}}/.^3) \end{bmatrix} \tag{23a}$$

$$\dot{\mathbf{q}}_k = \hat{\dot{\mathbf{q}}}_k + \begin{bmatrix} \frac{h}{2}\left(\breve{\mathbf{H}}_{\mathbf{f}}^{\mathrm{T}}\mathbf{f}_k - \breve{\mathbf{H}}_{\mathbf{f}}^{\mathrm{T}}\mathbf{f}_{k-1}\right) \\ \left(\tilde{\mathbf{H}}_{\mathbf{f}}^{\mathrm{T}}\mathbf{f}_k - \tilde{\mathbf{H}}_{\mathbf{f}}^{\mathrm{T}}\mathbf{f}_{k-1}\right).*\{\mathbf{n} - \cos(\tilde{\boldsymbol{\omega}}h)\}./(h\tilde{\boldsymbol{\omega}}.^2) \end{bmatrix} \tag{23b}$$

2.3. Inclusion of the gyroscopic effect

In order to include the gyroscopic effects, a vector $\mathbf{g}$ is introduced containing the gyroscopic moments, which, like the forces in $\mathbf{f}$, are considered as external to the non-rotating linear part. For the jth rotor ($j = 1,\ldots,J$) with speed $\Omega^{(j)}$ the gyroscopic effects are concentrated at G_j points. Hence,

$$\mathbf{g} = \mathbf{P}\dot{\boldsymbol{\theta}} \tag{24}$$

$\mathbf{P}$ is a block-diagonal matrix of diagonal sub-matrices $\mathbf{P}^{(j)} = \Omega^{(j)}\mathrm{diag}\{-I_1^{(j)}, I_1^{(j)}, \ldots, -I_{G_j}^{(j)}, I_{G_j}^{(j)}\}$, $\boldsymbol{\theta} = \{\boldsymbol{\theta}^{(j)}\}$, $\mathbf{g} = \{\mathbf{g}^{(j)}\}$, $\mathbf{g}^{(j)} = \begin{bmatrix} M_1^{(j)} & N_1^{(j)} & \cdots & M_{G_j}^{(j)} & N_{G_j}^{(j)} \end{bmatrix}^{\mathrm{T}}$, $\boldsymbol{\theta}^{(j)} = [\,\beta_1^{(j)} \quad \alpha_1^{(j)} \quad \cdots \quad \beta_{G_j}^{(j)} \quad \alpha_{G_j}^{(j)}\,]^{\mathrm{T}}$.

For the jth rotor: $I_p{}^{(j)}$ is the polar moment of inertia at location p ($p = 1,\ldots,G_j$); $M_p{}^{(j)}$, $\alpha_p{}^{(j)}$ are the gyroscopic moment and rotation respectively at location p about the x axis and $N_p{}^{(j)}$,$\beta_p{}^{(j)}$ are the gyroscopic moment and rotation, respectively, at location p about the y-axis (see the coordinate system of Fig. 1).

Extending Eqs. (12a, b):

$$\mathbf{x}_k = \hat{\mathbf{x}}_k + \mathbf{R}_{\mathbf{xf}}\{\mathbf{f}_k - \mathbf{f}_{k-1}\} + \mathbf{R}_{\mathbf{xg}}\{\mathbf{g}_k - \mathbf{g}_{k-1}\} \tag{25a}$$

$$\dot{\mathbf{x}}_k = \hat{\dot{\mathbf{x}}}_k + \mathbf{S}_{\mathbf{xf}}\{\mathbf{f}_k - \mathbf{f}_{k-1}\} + \mathbf{S}_{\mathbf{xg}}\{\mathbf{g}_k - \mathbf{g}_{k-1}\} \tag{25b}$$

$$\dot{\boldsymbol{\theta}}_k = \hat{\dot{\boldsymbol{\theta}}}_k + \mathbf{S}_{\boldsymbol{\theta}\mathbf{f}}\{\mathbf{f}_k - \mathbf{f}_{k-1}\} + \mathbf{S}_{\boldsymbol{\theta}\mathbf{g}}\{\mathbf{g}_k - \mathbf{g}_{k-1}\} \tag{25c}$$

where the matrices $\mathbf{R}_{\mathbf{xg}}$, $\mathbf{S}_{\mathbf{xg}}$, $\mathbf{S}_{\boldsymbol{\theta}\mathbf{f}}$, $\mathbf{S}_{\boldsymbol{\theta}\mathbf{g}}$ are obtained in a similar way to Eqs (22a, b), using modal vectors $\boldsymbol{\psi}_{\boldsymbol{\theta}}{}^{(r)}$, $\boldsymbol{\psi}_{\mathbf{g}}{}^{(r)}$ taken at the degrees of freedom corresponding to the elements in $\boldsymbol{\theta}$ and $\mathbf{g}$, respectively, and

$$\dot{\boldsymbol{\theta}}_k = \mathbf{H}_{\boldsymbol{\theta}}\dot{\mathbf{q}}_k,\ \hat{\dot{\boldsymbol{\theta}}}_k = \mathbf{H}_{\boldsymbol{\theta}}\hat{\dot{\mathbf{q}}}_k \tag{26a,b}$$

$$\mathbf{H}_{\boldsymbol{\theta}} = \begin{bmatrix} \boldsymbol{\psi}_{\boldsymbol{\theta}}^{(1)} & \cdots & \boldsymbol{\psi}_{\boldsymbol{\theta}}^{(R)} \end{bmatrix}^{\mathrm{T}} = \begin{bmatrix} \breve{\mathbf{H}}_{\boldsymbol{\theta}} & \tilde{\mathbf{H}}_{\boldsymbol{\theta}} \end{bmatrix}, \quad \mathbf{H}_{\mathbf{g}} = \begin{bmatrix} \boldsymbol{\psi}_{\mathbf{g}}^{(1)} & \cdots & \boldsymbol{\psi}_{\mathbf{g}}^{(R)} \end{bmatrix}^{\mathrm{T}} = \begin{bmatrix} \breve{\mathbf{H}}_{\mathbf{g}} & \tilde{\mathbf{H}}_{\mathbf{g}} \end{bmatrix} \tag{27a,b}$$

Using Eq. (24) in Eq. (25c) and rearranging

$$\dot{\boldsymbol{\theta}}_k = \mathbf{L}\hat{\dot{\boldsymbol{\theta}}}_k + \mathbf{L}\mathbf{S}_{\boldsymbol{\theta}\mathbf{f}}\{\mathbf{f}_k - \mathbf{f}_{k-1}\} - \mathbf{L}\mathbf{T}\dot{\boldsymbol{\theta}}_{k-1} \tag{28}$$

where

$$\mathbf{L} = \mathbf{L}(h, \Omega^{(1,\ldots,J)}) = [\mathbf{I} - \mathbf{T}]^{-1}, \quad \mathbf{T} = \mathbf{T}(h, \Omega^{(1,\ldots,J)}) = \mathbf{S}_{\boldsymbol{\theta}\mathbf{g}}(h)\mathbf{P} \tag{29a,b}$$

…$\mathbf{I}$ being the identity matrix. Hence, using Eq. (24) in Eqs. (25a, b) and substituting Eq. (28):

$$\mathbf{x}_k = \hat{\mathbf{x}}_k + \mathbf{R}_{\mathbf{xg}}\mathbf{P}\mathbf{L}\hat{\dot{\boldsymbol{\theta}}}_k - \{\mathbf{R}_{\mathbf{xg}}\,\mathbf{P}\mathbf{L}\mathbf{T} + \mathbf{R}_{\mathbf{xg}}\mathbf{P}\}\dot{\boldsymbol{\theta}}_{k-1} + \{\mathbf{R}_{\mathbf{xf}} + \mathbf{R}_{\mathbf{xg}}\mathbf{P}\mathbf{L}\mathbf{S}_{\boldsymbol{\theta}\mathbf{f}}\}\{\mathbf{f}_k - \mathbf{f}_{k-1}\} \tag{30a}$$

$$\dot{\mathbf{x}}_k = \hat{\dot{\mathbf{x}}}_k + \mathbf{S}_{\mathbf{xg}}\,\mathbf{P}\mathbf{L}\hat{\dot{\boldsymbol{\theta}}}_k - \left\{\mathbf{S}_{\mathbf{xg}}\,\mathbf{P}\mathbf{L}\mathbf{T} + \mathbf{S}_{\mathbf{xg}}\,\mathbf{P}\right\}\dot{\boldsymbol{\theta}}_{k-1} + \{\mathbf{S}_{\mathbf{xf}} + \mathbf{S}_{\mathbf{xg}}\mathbf{P}\mathbf{L}\mathbf{S}_{\boldsymbol{\theta}\mathbf{f}}\}\{\mathbf{f}_k - \mathbf{f}_{k-1}\} \tag{30b}$$

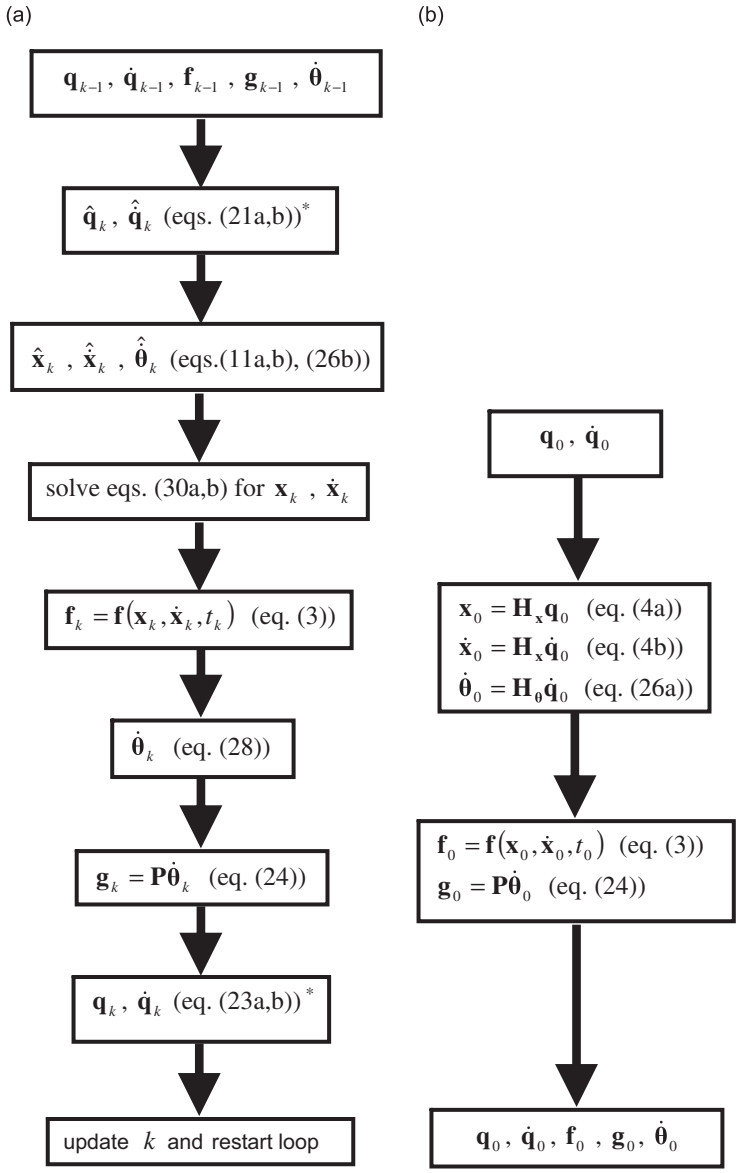

Fig. 3. Flow chart of IRM computational sequence: (a) loop ($k = 1,2,\ldots$), (b) starting sequence. *See note on penultimate paragraph of Section 2.3.

The above Eqs. (30a, b) now replace Eqs. (12a, b) and are solved for $\mathbf{x}_k, \dot{\mathbf{x}}_k$ in the same way. One can use the sum of the first three terms in each equation as a first approximation. $\dot{\boldsymbol{\theta}}_k$ is then updated according to Eq. (28). Eqs. (23a, b) are then used to determine $\mathbf{q}_k, \dot{\mathbf{q}}_k$ and progress the solution.

The IRM computational sequence is illustrated in Fig. 3. For $k = 1$, the data $\mathbf{f}_{k-1}$, $\mathbf{g}_{k-1}$, $\dot{\boldsymbol{\theta}}_{k-1}$, in the first block of the loop in Fig. 3a are generated by the starting sequence depicted in Fig. 3b. It is noted that Eqs. (21a, b) and (23a, b) are to be used with the terms $\breve{\mathbf{H}}_\mathbf{f}^\mathrm{T}\mathbf{f}_k$, $\breve{\mathbf{H}}_\mathbf{f}^\mathrm{T}\mathbf{f}_{k-1}$, $\tilde{\mathbf{H}}_\mathbf{f}^\mathrm{T}\mathbf{f}_k$, $\tilde{\mathbf{H}}_\mathbf{f}^\mathrm{T}\mathbf{f}_{k-1}$ replaced by $\breve{\mathbf{H}}_\mathbf{f}^\mathrm{T}\mathbf{f}_k + \breve{\mathbf{H}}_\mathbf{g}^\mathrm{T}\mathbf{g}_k$, $\breve{\mathbf{H}}_\mathbf{f}^\mathrm{T}\mathbf{f}_{k-1} + \breve{\mathbf{H}}_\mathbf{g}^\mathrm{T}\mathbf{g}_{k-1}$, $\tilde{\mathbf{H}}_\mathbf{f}^\mathrm{T}\mathbf{f}_k + \tilde{\mathbf{H}}_\mathbf{g}^\mathrm{T}\mathbf{g}_k$, $\tilde{\mathbf{H}}_\mathbf{f}^\mathrm{T}\mathbf{f}_{k-1} + \tilde{\mathbf{H}}_\mathbf{g}^\mathrm{T}\mathbf{g}_{k-1}$, respectively.

Finally, it is to be noted that any concentrated viscous damping elements can be dealt with in a similar manner to the gyroscopic moments, without affecting the size of the problem.

3. Simulations

The computational method was applied to a representative twin-spool aero-engine having the schematic layout in Fig. 1, using a realistically sized whole-engine FE model provided by an engine manufacturer. Fig. 2 illustrates the overall computational procedure. All simulations were performed in Matlab on a standard 2006-issue desktop pc with Intel® Pentium® D CPU 3 GHz processor.

3.1. Linear pre-processing

In order to assess the influence of the computed modes, the frequency response functions (receptances) of the undamped linear part for zero rotational speed were computed from the modal parameters. Fig. 4 shows the y displacement at B_1 (Fig. 1) per unit y force at the same point over the range 0 to 1 kHz, which contains a total of 934 modes. It is clear that there is a high modal density at relatively low frequencies, considering that the high pressure (HP) shaft runs at speeds up to 16,000 rev/min and that the nonlinear response will contain engine orders. One should note that the sudden reduction in modal density beyond 500 Hz is merely an artefact of the degree-of-freedom reduction technique used by the FE modellers.

This exercise clearly shows that, for the nonlinear processing, an attempt at time-saving by integrating a restricted number of modal equations is not advisable. The use of a residual flexibility technique [8] is not helpful since this only corrects the static influence of truncated high-frequency modes. Moreover, any attempt at sifting out some of those low-frequency modes deemed not to significantly affect the vibration is bound to be both time-consuming and prone to significant errors. It is for this reason that certain whole-engine modelling specialists actually opt for the highly time-consuming direct integration of the FE equations (i.e. in physical coordinates).

3.2. Nonlinear computation for the unbalance response

Fig. 5 gives information relating to the constituents of the force vector $\mathbf{f}$ in Eq. (3). This vector contains a static sub-vector defining the distributed weights of the two rotors.

The motion dependence of $\mathbf{f}$ is due to the sub-vector of SFD forces $\boldsymbol{\rho} = [\boldsymbol{\rho}_1^{\mathrm{T}} \quad \cdots \quad \boldsymbol{\rho}_5^{\mathrm{T}}]^{\mathrm{T}}$ where $\boldsymbol{\rho}_i = [Q_{x_i} \quad Q_{y_i}]^{\mathrm{T}}$ defines the Cartesian forces at SFD no. i. Now $\boldsymbol{\rho}_i = \boldsymbol{\rho}_i(\mathbf{v}_i, \dot{\mathbf{v}}_i)$ [6] where the vector $\mathbf{v}_i$ defines the instantaneous Cartesian displacements of J_i relative to B_i (see Fig. 1):

$$\mathbf{v}_i = \mathbf{v}_{\mathrm{s},i} + [x_{\mathrm{d},i} \quad y_{\mathrm{d},i}]^{\mathrm{T}} \tag{31}$$

$\mathbf{v}_{\mathrm{s},i}$ defines the static offset of J_i relative to B_i in the x, y directions (under no rotor loading). The vector $\mathbf{x}$ in Section 2 comprises the *dynamic* components of the relative displacements in Eq. (31), i.e.

$$\mathbf{x} = \begin{bmatrix} x_{\mathrm{d},1} & y_{\mathrm{d},1} & \cdots & x_{\mathrm{d},5} & y_{\mathrm{d},5} \end{bmatrix}^{\mathrm{T}} \tag{32}$$

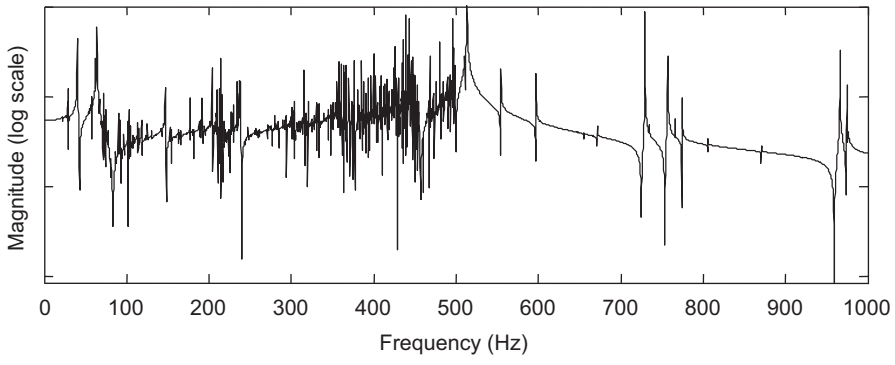

Fig. 4. Point receptance frequency response at point B_1 in the y direction.

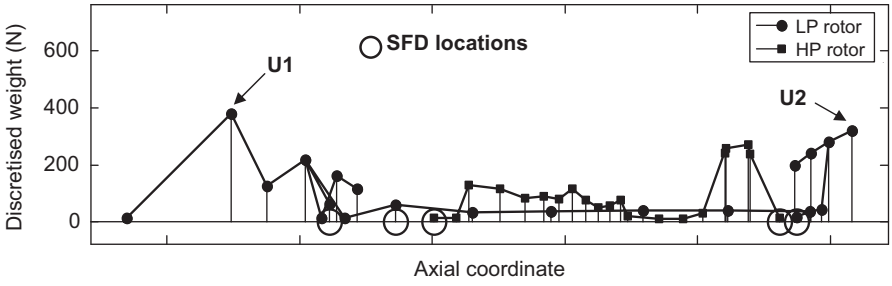

Fig. 5. Rotor weight distribution, unbalance locations, and bearing locations.

The SFDs considered for this illustrative study were single-land and end-fed with oil of viscosity $0.0049\,\mathrm{N\,s\,m^{-2}}$ at a pressure of 3 bar (gauge). The bearing diameters and radial clearances were typically 200, 0.1 mm, respectively, and the land lengths ranged from 16 to 34 mm. As in current industrial practice, the instantaneous pressure distribution in each SFD was approximated by a combining the short and long bearing expressions through an "end-leakage factor" λ representing the degree of end-sealing [12]. Each distribution was truncated below a cavitation pressure of absolute zero (-101.325 kPa) and numerically integrated across the oil film to yield the associated SFD forces [6]. For these preliminary calculations, the bearing housings were assumed to be perfectly aligned with each other prior to rotor assembly (i.e. $\mathbf{v}_{s,i}=0$, $i=1,\ldots,5$).

For all simulations presented in this paper, the unbalance was restricted to two locations U1 and U2 on the low-pressure (LP) rotor as shown in Fig. 5. The unbalance mass–radius products at these locations were set to be 6.3 g in-phase. The rotational speeds of both rotors were 10,000 rev/min in the same sense (i.e. co-rotation).

The gyroscopic effect was discretised at 7 points on the LP rotor and 12 points on the HP rotor.

3.2.1. Testing and validation of IRM

An unbalance response problem was solved in two ways: (i) IRM; (ii) "CIM": the conventional implicit integration of the modal equations (1) using the solver *ode23s*© [9] available in the Matlab package. In either case, all 934 modes were considered. In the case of method (ii) Eqs. (1) were cast in the standard form $\dot{\mathbf{s}}=\boldsymbol{\chi}(t,\mathbf{s})$ where $\mathbf{s}$ is the vector of modal state variables $\mathbf{q}$, $\dot{\mathbf{q}}$, and $\boldsymbol{\chi}$ is a vector function of $\mathbf{s}$ and t. Both methods required a Jacobian matrix at each time step. Method (i) (IRM) required the Jacobian of Eqs. (30a,b) for solution by the Newton–Raphson method. During the iterative process at a given time step, the inverse of the Jacobian was updated using Broyden's method [13]. In the case of method (ii) (CIM), the solver was supplied with a user-derived expression for the Jacobian $\partial\boldsymbol{\chi}/\partial\mathbf{s}$, as recommended in Ref. [9], since this considerably accelerated the solution compared to letting the solver compute the Jacobian from first principles. Although the required Jacobians were different for the two methods (i, ii), in either case the effort in the Jacobian computation lay in the calculation of the partial derivatives of the SFD forces with respect to the associated relative displacements and velocities (as can be seen in Ref. [14] for the case of CIM). The SFD force partial derivatives calculation was performed in both methods (i, ii) by the same routine. Hence, the ensuing differences in computational speed were attributable purely to the different time-marching algorithms.

Both solvers used an adaptive control of the time step-size h in order to efficiently maintain the numerical error within a prescribed tolerance. In the case of the IRM, the iterative solution of Eqs. (30a, b) at a given time step was deemed successful if, among other conditions, the magnitude of the difference between consecutive iterates fell below the prescribed tolerance and the solution was completed within a set number of iterations. An estimate for a new step-size $h_{\mathrm{new,est}}$ was computed on the basis of the degree of convergence obtained with the previous step-size. In order to save time, the programme had the facility to pick a step-size closely matching $h_{\mathrm{new,est}}$ from a range of discrete step-sizes for which those matrices in Eqs. (30a, b) that depend on h (like $\mathbf{R_{xf}}$, $\mathbf{S_{xf}}$, etc.) had been pre-computed at the start of the time-marching procedure.

Figs. 6 and 7 show that the results obtained by the two methods are in excellent agreement, and that the IRM was found to be at least 40 times faster than the CIM. The number of equations solved by CIM at each time step was 934×2, whereas the number of equations to be solved by the IRM was fixed at a mere 20, regardless of the number of modes included. For the tolerance setting used to obtain the IRM results in

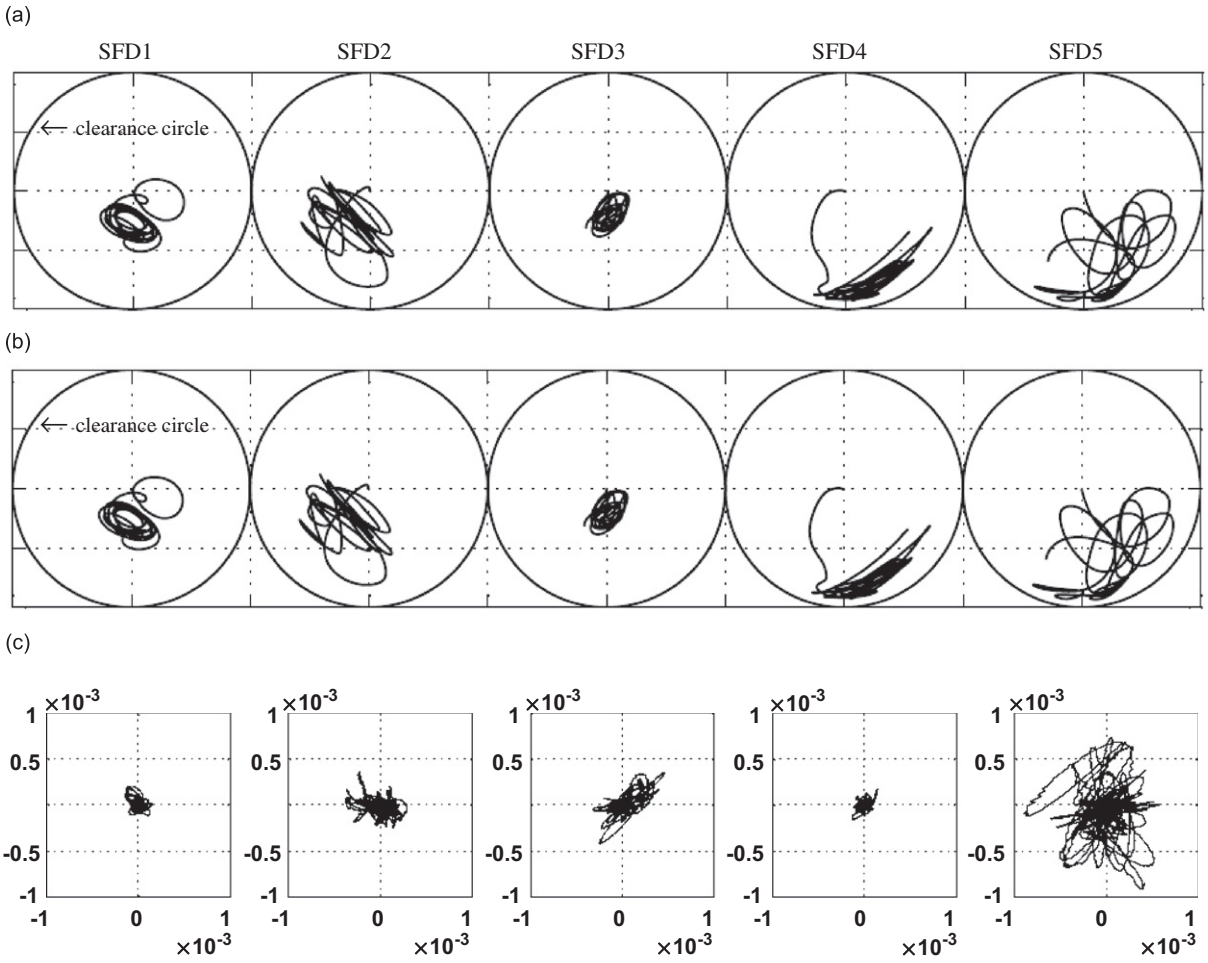

Fig. 6. Validation of IRM against CIM: first 10 LP-shaft revs. (a) Relative orbits of journals within the respective clearance circles by CIM (CPU time: 86 mins), (b) relative orbits of journals within the respective clearance circles by IRM (CPU time: 2 mins) and (c) difference between CIM and IRM orbits (normalised with respect to corresponding radial clearance).

Fig. 6b, the difference graphs in Fig. 6c were invariant for tolerance settings of the CIM solver below 1% of the average radial clearance (the CIM computational time quoted in Fig. 6a is for this latter tolerance). For coarser tolerance settings of the CIM, the difference was greater than that shown in Fig. 6c. This suggests that the IRM has also the potential for greater numerical accuracy. The reason for this is that the unknowns of the algebraic equations solved by the CIM are the modal state variables $\mathbf{q}, \dot{\mathbf{q}}$. Hence, in order to obtain the relative displacements and velocities necessary to evaluate the SFD forces, the CIM had to perform a modal transformation each time. The CIM solver applies its prescribed tolerance to the modal state variables, rather than the relative displacements and velocities at the SFDs. On the other hand, the IRM equations (30a, b) are directly formulated in terms of the relative displacements and velocities at the SFDs.

Fig. 7 shows that the close agreement between the two methods was maintained as the solution was progressed. More simulations performed at other LP rotors speeds also showed that the IRM was at least 40 times faster than the CIM.

3.2.2. *Some preliminary results of a parametric analysis*

Fig. 8 shows the final steady-state orbits for the above-discussed simulations, for which the end-leakage factor $\lambda = 0.03$ (typical value used for engine simulations in industry). SFDs 1, 2, and 5 were on the LP shaft, which carried the unbalance. Vibration transmission between the two rotors is through the bearing housings,

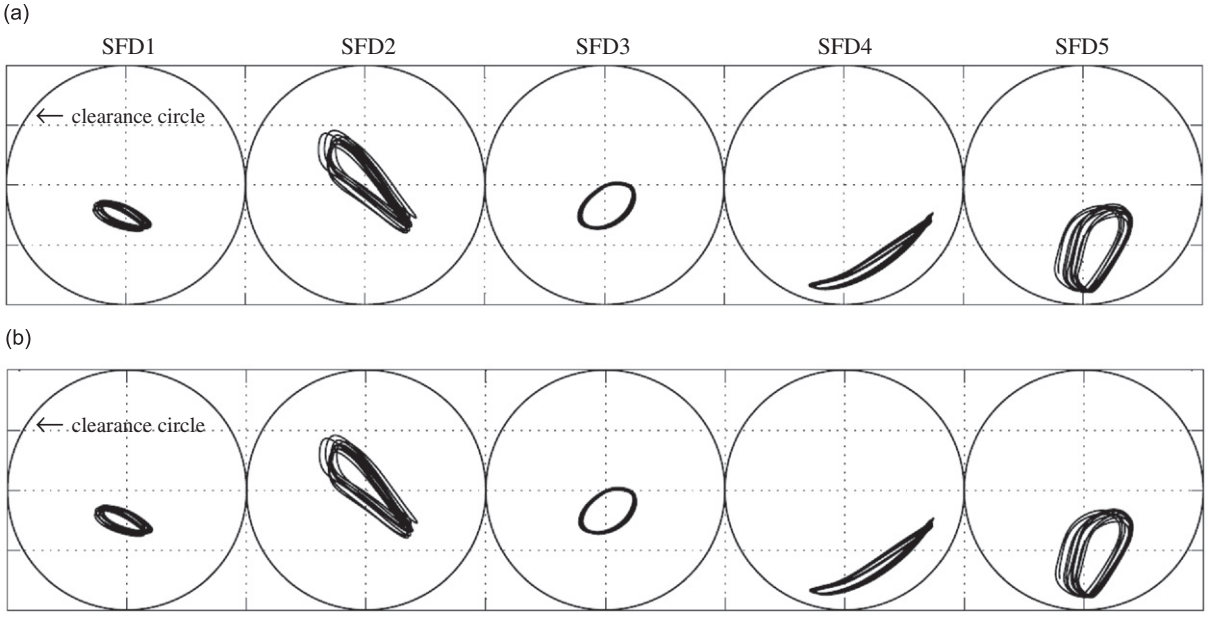

Fig. 7. Validation of IRM against CIM: last 10 out of first 100 LP-shaft revs. (a) Relative orbits of journals within the respective clearance circles by CIM and (b) relative orbits of journals within the respective clearance circles by IRM.

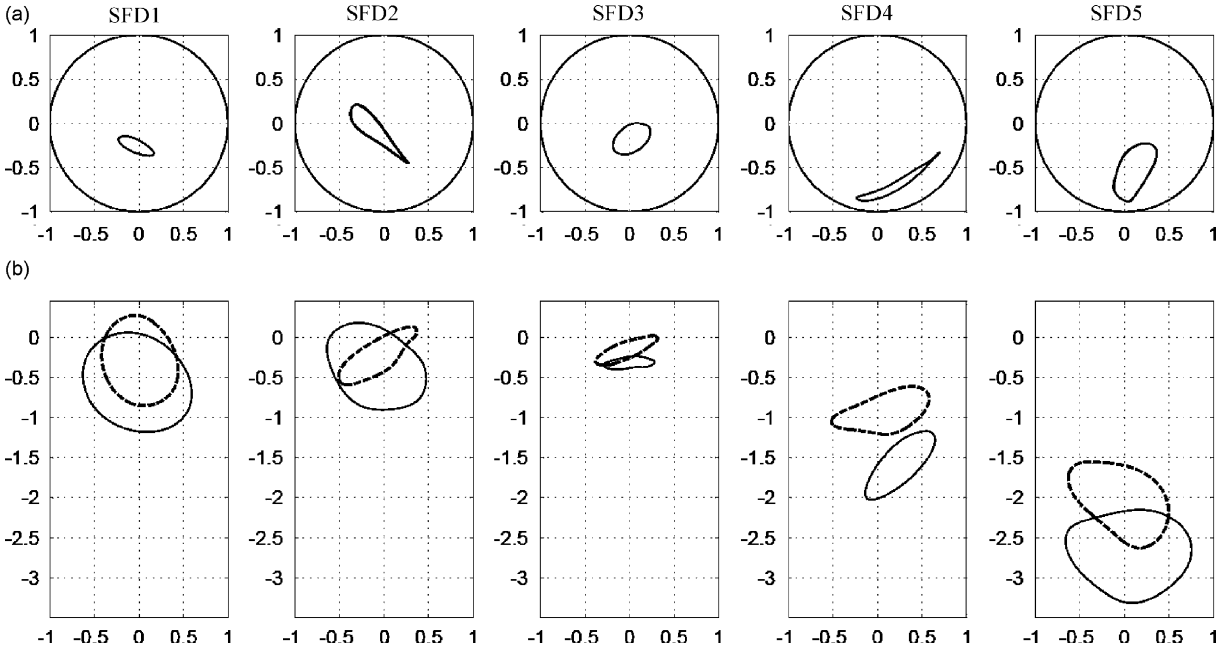

Fig. 8. Steady-state orbits for $\lambda = 0.03$: last five out of first 4000 LP-shaft revs. (a) Relative orbits of journals within the respective clearance circles and (b) absolute orbits of journal (—) and housing (- - -) centres.

whose vibration is shown in Fig. 8b. It is to be noted that SFDs 1 and 3 were spring-supported and the orbit offsets within the clearances of these SFDs were mainly due to the respective rotor weights. The size, shape and position of the orbits at the other (unsupported) SFDs were influenced by their static and dynamic loading. Fig. 9 shows that the steady-state vibration was also periodic for a lower degree of sealing of $\lambda = 0.015$ (all other parameters kept the same). The orbits in Figs. 8 and 9 described periodic vibration with a

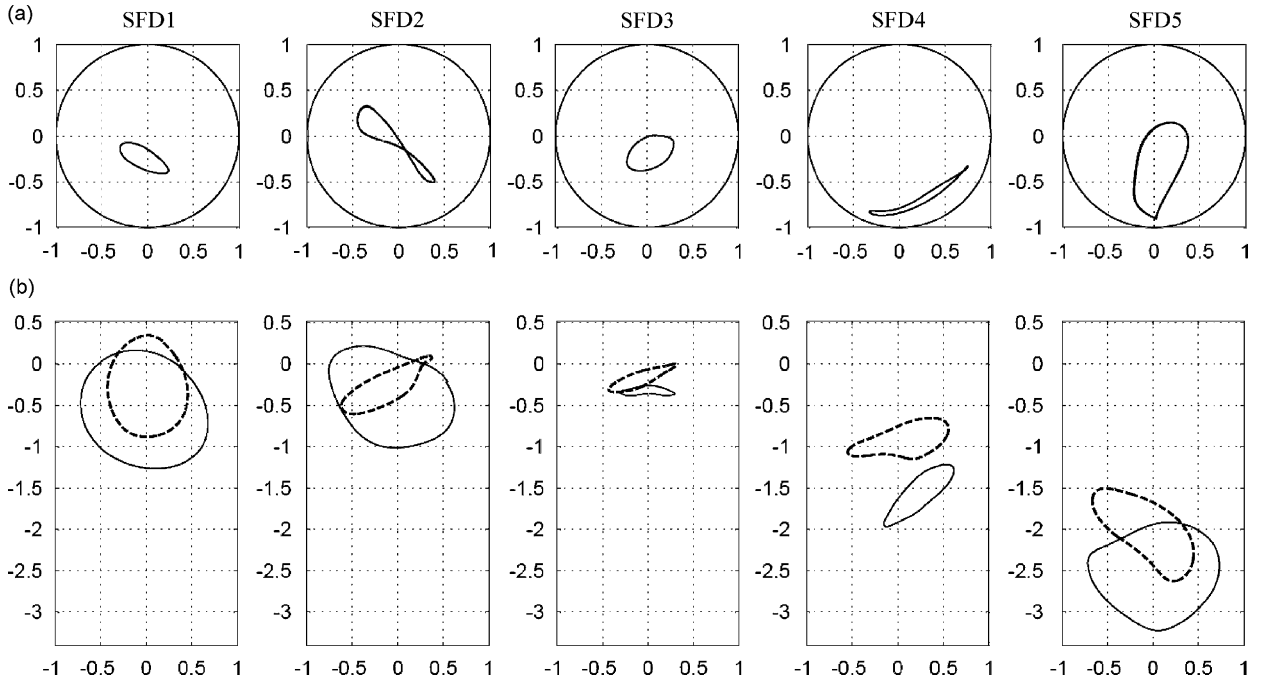

Fig. 9. Steady-state orbits for $\lambda = 0.015$: last five out of first 4000 LP-shaft revs. (a) Relative orbits of journals within the respective clearance circles and (b) absolute orbits of journal (—) and housing (- - -) centres.

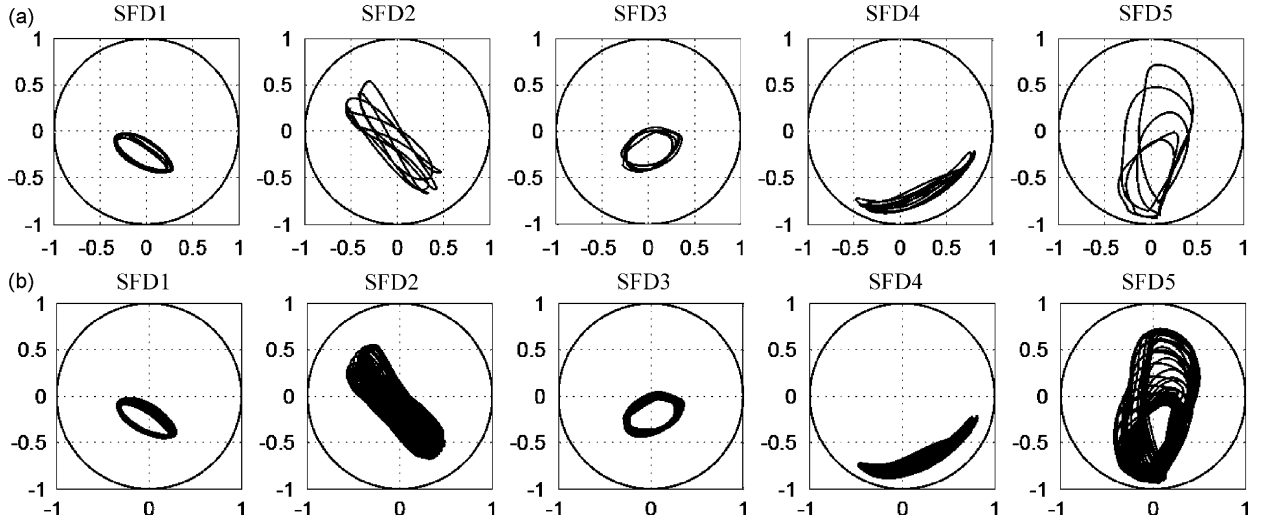

Fig. 10. Steady-state relative orbits of journals within the respective clearance circles for $\lambda = 0.01$. (a) Last 5 out of first 4000 LP-shaft revs and (b) last 50 out of first 4000 LP-shaft revs (orbits normalised with respect to corresponding radial clearances).

fundamental frequency equal to the rotational speed of the unbalanced rotor. As the end-leakage factor was further reduced to $\lambda = 0.010$ no such periodic orbits were obtained after several thousand revolutions, as can be seen in Figs. 10a and b. Hence, it appears that, for the unbalance distribution and rotational speed considered, the nature of the predicted engine vibration changes from periodic to quasi-periodic as the degree of sealing is reduced to a very low level. Such aperiodic vibration is similar to that predicted and measured on other, much simpler, systems with unsealed (i.e. $\lambda \to 0$) SFD bearings e.g. Refs. [6,7].

4. Conclusions

A novel implicit "IRM" has been developed for the time domain computation of the vibration of a whole-engine model with nonlinear bearings. The IRM's computational efficiency is largely immune to the number of modes used and dependent only on the number of nonlinear elements. This means that, apart from retaining numerical accuracy, a much more physically accurate solution is achievable within a short timeframe. Simulation tests on a realistically sized representative twin-spool engine showed that the new method was around 40 times faster than a conventional implicit integration scheme. Preliminary results illustrated the varying degree of lift and orbit size at the SFD bearings for given unbalance distribution, and the effect of sealing. The new method is of course equally applicable with other types of concentrated nonlinearities and should greatly facilitate the hitherto highly restricted nonlinear dynamic analysis of realistic engine structures.

Acknowledgements

The authors acknowledge the support of the EPSRC of the UK and the support of Rolls-Royce plc.

References

[1] R. Holmes, M.M. Dede, Non-linear phenomena in aero-engine rotor vibration, *Proceedings of the Institution of Mechanical Engineers Part G Journal of Aerospace Engineering* 203 (1989) 25–34.
[2] C.L. Lim, D.F. Kik, M.C. Levesley, Analysis of a flexible rotor system including non-linear squeeze film damping using a finite element method, *IMechE Conference Transactions, Eighth International Conference on Vibrations in Rotating Machinery*, University of Wales, Swansea, UK, 7–9 September 2004, pp. 131–140 (Professional Engineering Publishing).
[3] Z. Gu, X. Zhi, G. Meng, T. Fang, Transient response analysis of large-scale rotor-bearing system with strong non-linear elements by a transfer matrix-Newmark formulation integration method, *Journal of Sound and Vibration* 259 (3) (2003) 559–570.
[4] F. Chu, R. Holmes, Efficient computation on the nonlinear responses of a rotating assembly incorporating the squeeze-film damper, *Computer Methods in Applied Mechanical Engineering* 164 (1998) 363–373.
[5] R.W. Armentrout, E.J. Gunter, Transient modal analysis of nonlinear rotor-bearing systems, *SPIE Proceedings* 3727 (1) (1999) 290–296.
[6] P. Bonello, M.J. Brennan, R. Holmes, Non-linear modelling of rotor dynamic systems with squeeze film dampers—an efficient integrated approach, *Journal of Sound and Vibration* 249 (4) (2002) 743–773.
[7] P. Bonello, M.J. Brennan, R. Holmes, The prediction of the non-linear dynamics of a squeeze film damped aero-engine rotor housed in a flexible support structure, *Proceedings of the Institute of Mechanical Engineers Part G Journal of Aerospace Engineering* 218 (3) (2004) 213–230.
[8] M. Petyt, *Introduction to Finite Element Vibration Analysis*, Cambridge University Press, Cambridge, UK, 1998.
[9] L.F. Shampine, M.W. Reichelt, The Matlab ODE suite, *SIAM Journal on Scientific Computing* 18 (1) (1997) 1–22.
[10] R.E.D. Bishop, D.C. Johnson, *The Mechanics of Vibration*, Cambridge University Press, Cambridge, UK, 1960.
[11] Matlab®. The Mathworks, Inc., Natick, MA, USA, 2006.
[12] M.M. Dede, M. Dogan, R. Holmes, The damping capacity of a sealed squeeze film bearing, *Journal of Tribology—Transactions of the ASME* 107 (1985) 411–418.
[13] G. Dahlquist, *Numerical Methods*, Prentice-Hall, Englewood Cliffs, NJ, 1974.
[14] P. Bonello, Transient modal analysis of the nonlinear dynamics of a turbocharger, *Ninth International Conference on Vibrations in Rotating Machinery*, University of Exeter, UK, September 2008, Paper no. C663/006/2008.